Spectrochimica Acta Part A: Molecular and Biomolecular Spectroscopy 153 (2016) 746–753

Contents lists available at ScienceDirect

Spectrochimica Acta Part A: Molecular and Biomolecular Spectroscopy

journal homepage: www.elsevier.com/locate/saa

A rhenium complex doped in a silica molecular sieve for molecular oxygen sensing: Construction and characterization

Xiaozhou Yang [a,*], Yanxiao Li [b]

[a] School of Physics and State Key Laboratory of Nuclear Physics and Technology, Peking University, Beijing 100871, China
[b] School of Materials Science and Engineering, Zhejiang University, Hangzhou 310058, China

ARTICLE INFO

Article history:
Received 7 August 2015
Received in revised form 15 September 2015
Accepted 27 September 2015
Available online 30 September 2015

Keywords:
Re(I) complex
Oxygen-sensing
Photophysical features
MCM-41
Theoretical analysis

ABSTRACT

This paper reported a diamine ligand and its Re(I) complex for potential application in oxygen sensing. The novelty of this diamine ligand localized at its increased conjugation chain which had a typical electron-withdrawing group of 1,3,4-oxadiazole. Electronic distribution of excited electrons and their lifetime were supposed to be increased, favoring oxygen sensing collision. This hypothesis was confirmed by single crystal analysis, theoretical calculation and photophysical measurement. It was found that this Re(I) complex had a long-lived emission peaking at 545 nm, favoring sensing application. By doping this complex into a silica matrix MCM-41, oxygen sensing performance and mechanism of the resulting composites were discussed in detail. Non-linear Stern–Volmer working curves were observed with maximum sensitivity of 5.54 and short response time of ~6 s.

1. Introduction

Recently, composite materials, such as organic–inorganic hybrid ones, have harvested many research interests because they collect and hold features of each component, showing improved performance over that of pure counterparts [1,2]. Generally, the organic component in a composite material is designed as functional part since it can be readily modified to meet application requirements. While the inorganic component is usually chosen as supporting matrix for functional part in virtue of its good mechanical strength and stability [2,3]. To properly combine organic and inorganic components, various hybrid structures have been proposed to satisfy applications in optical sensing, solar cells, optoelectronic devices, catalysts and so on.

Among these potential applications, optical sensing is interesting owing to its advantages of quick response and limited requirement for instrumentation. Molecular O_2 is usually considered as an important analyte since its recognition/quantification is a key problem in chemical industry/engineering, food processing, medicine and environmental protection [5,6]. Compared to classical techniques such as Winkler titration and Clark electrode approach, optical oxygen sensing has shown virtues of no analyte consumption, simple pre-treatment and low need for instrumentation, making itself a good candidate for on-line and in-field monitoring [7,8].

For a representative composite material for oxygen sensing, there are two major components, supporting matrix and sensing probe [9–12]. Supporting matrix disperses probe molecules and allows smooth analyte diffusion, favoring fast and linear response. Some criteria, such as high diffusion coefficient, photostability and compatibility with probe, should be met so that smooth analyte transportation, reliable signal output and homogeneous sensing could be achieved. A silica molecular sieve MCM-41 has been highly recommended since it satisfies these criteria well [11,12].

As for sensing probe, long-lifetime and wide distribution of excited electrons are usually desired to guarantee enough collision chances with analyte. It seems that transition metal complexes, especially Re(I)-based ones, can well satisfy above requirements [13–16]. Theoretical calculation has pointed out that their electrons in ground state are localized at metal center, while electrons in their first excited state are centralized at diamine ligand π^*, making their onset electronic transition a metal-to-ligand-charge-transfer (MLCT) one. By increasing π^* of diamine ligands, distribution of excited electrons may be widened, meeting the requirement for an ideal probe. In addition, electron-withdrawing groups are positive to increase lifetime of emissive center by decreasing non-radiative decay probability [13–16].

Guided by above consideration, this paper intends to develop a diamine ligand with a typical electron-withdrawing group of 1,3,4-oxadiazole. Π^* conjugation area of this ligand is supposed to be increased. Photophysical feature of its corresponding Re(I) complex is analyzed and discussed in detail. By doping this Re(I) complex into MCM-41, its spectral response to O_2 is investigate1d as well.

---

[*] Corresponding author.
E-mail address: yangxz615@163.com (X. Yang).

http://dx.doi.org/10.1016/j.saa.2015.09.034
1386-1425/

2. Experimental details

2.1. General information for reagents and apparatus

Synthetic route for our diamine ligand, its Re(I) complex and the final composites is shown in Scheme 1. Starting compound 2-(2H-tetrazol-5-yl)-pyridine (TP) was synthesized following a literature procedure [17]. Other reagents, such as benzoyl chloride, sodium azide, MCM-41, zinc bromide, and $Re(CO)_5Br$, were obtained from Yunzi Chemical Co. (Hangzhou) and used without further purifications. Organic solvents were purified with standard procedures.

NMR, MS, UV–vis absorption, and emission spectra were recorded by a Varian INOVA 300 spectrometer, a Agilent 1100 MS series/AXIMA CFR MALDI/TOF MS spectrometer, a Shimadzu UV-3101PC spectrophotometer and a Hitachi F-4500 fluorescence spectrophotometer, respectively. Elemental analysis was finished on a Vario Element Analyzer. Excited state decay dynamics were recorded by a two-channel TEKTRONIX TDS-3052 oscilloscope, using pulsed Nd:YAG laser as excitation source ($\lambda = 355$ nm). Scanning electron microscopy (SEM) image was obtained by a Hitachi S-4800 microscope. Small-angle X-ray diffraction (SAXRD) patterns were recorded by a Rigaku-Dmax 2500 diffractometer ($\lambda = 0.154$ nm, scanning step $= 0.02°$). Single crystal was analyzed on a Siemens P4 single-crystal X-ray diffractometer equipped with a Smart CCD-1000 detector and graphite-monochromated Mo Kα radiation (50 kV, 30 A, 298 K). All hydrogen atoms were calculated. Density functional theory calculation was performed on this single crystal by GAMESS at RB3LYP1/SBKJC level. Graphical presentation for frontier molecular orbitals was generated by wxMacMolPlt with contour value of 0.025.

2.1. Synthesis of diamine ligand POP

Diamine ligand POP was synthesized following below procedure. TP (20 mmol), benzoyl chloride (22 mmol) and anhydrous pyridine (25 mL) were mixed together under N_2 protection, heated to reflux and kept for 60 h. After cooling, cold water (200 mL) was added. The resulting crude product was collected and purified on a silica gel column. ^1H NMR (300 MHz, $CDCl_3$): δ 7.38 (1H, m), 7.51 (3H, m), 7.87 (1H, m), 8.14 (1H, t), 8.21 (1H, t), 8.28 (1H, d, $J = 6.0$), 8.69 (1H, d, $J = 3.5$). Anal. Calcd. for $C_{13}H_9N_3O$: C, 69.95; H, 4.06; N, 18.82. Found: C, 69.88; H, 4.21; N, 18.67. MS m/z: $[m]^+$ calc. for $C_{13}H_9N_3O$, 223.1; found, 223.0.

2.2. Synthesis of Re(I) complex $Re(CO)_3(POP)Br$

Re(I) complex $Re(CO)_3(POP)Br$ was synthesized following below procedure. POP (1 mmol), $Re(CO)_5Br$ (1 mmol) and toluene (20 mL) were mixed together under N_2 protection, heated to reflux and kept for 6 h. After cooling, solvent was extracted by rotary evaporation. The resulting crude product was collected and purified on a silica gel column. ^1H NMR (300 MHz, $CDCl_3$): δ 7.52 (1H, m), 7.67 (3H, m), 7.85 (1H, m), 8.24 (1H, t), 8.29 (1H, t), 8.37 (1H, d, $J = 6.0$), 8.87 (1H, d, $J = 4.0$). Anal. Calcd. for $C_{16}H_9BrN_3O_4Re$: C, 33.52, H, 1.58, N, 7.33. Found: C, 33.64, H, 1.67, N, 7.22. MS m/z: $[m]^+$ calc. for $C_{16}H_9BrN_3O_4$, 572.9; found, 573.0. Its identity was further confirmed by single crystal XRD analysis (CCDC 1086734).

2.3. Construction of composites $Re(CO)_3(POP)Br$ doped MCM-41

Our sensing composites were constructed by doping various amounts of $Re(CO)_3(POP)Br$ into molecular sieve MCM-41 [17,18]. A typical run is described as follows. Dopant $Re(CO)_3(POP)Br$ was carefully weighed and dissolved into CH_2Cl_2 (5 mL) under stirring. When solution became clear, MCM-41 (1 g) was added into the solution and stirred for 30 min. Then solid product was collected and washed with CH_2Cl_2 (10 mL × 3), giving $Re(CO)_3(POP)Br$ doped MCM-41 as pale orange powder.

3. Results and discussion

3.1. Molecular structure of probe $Re(CO)_3(POP)Br$

Aiming at a better understanding on probe, we are giving a brief explanation on its molecular structure. For a typical transition metal complex, it has been found that electrons of its first excited state are localized on diamine ligand π^*, which makes them vulnerable to energy acceptors [15–17]. As shown in Scheme 1, there is a large conjugation plane in POP ligand. With its wide ligand π^*, excited electrons may be readily attacked by O_2 molecules. In addition, this large conjugation plane may depress non-radiative decay probability and thus improve emission performance [13–16]. Small ligands of CO and Br are positive to decrease steric hindrance when being attacked by O_2 molecules. These factors make $Re(CO)_3(POP)Br$ a promising oxygen sensing probe.

Above hypothesis is firstly confirmed by the single crystal structure of $Re(CO)_3(POP)Br$ shown in Fig. 1. Its key structural parameters are

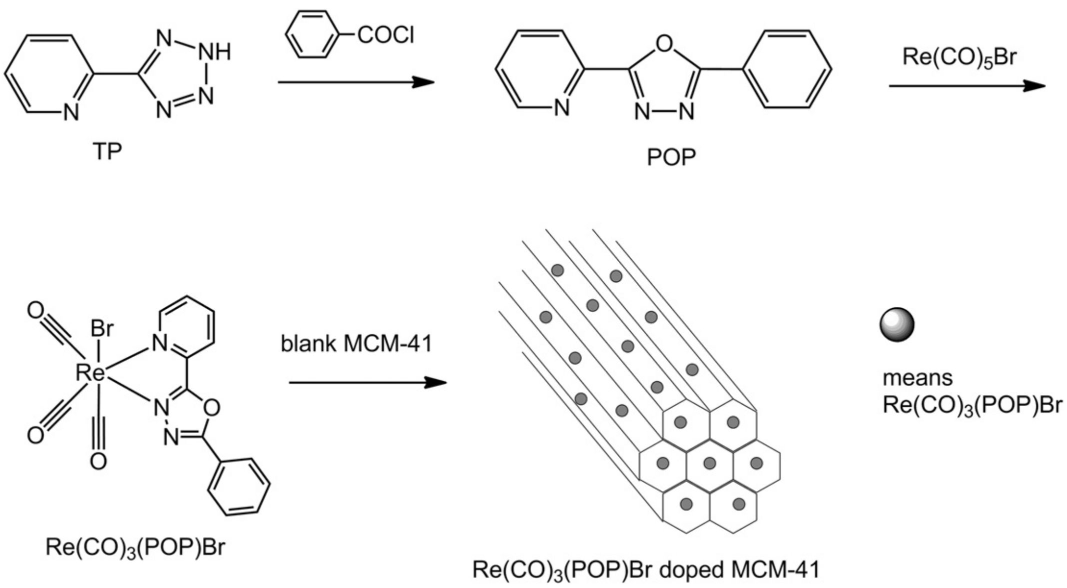

Scheme 1. Synthetic route for ligand POP, corresponding Re(I) complex $Re(CO)_3(POP)Br$ and $Re(CO)_3(POP)Br$ doped MCM-41.

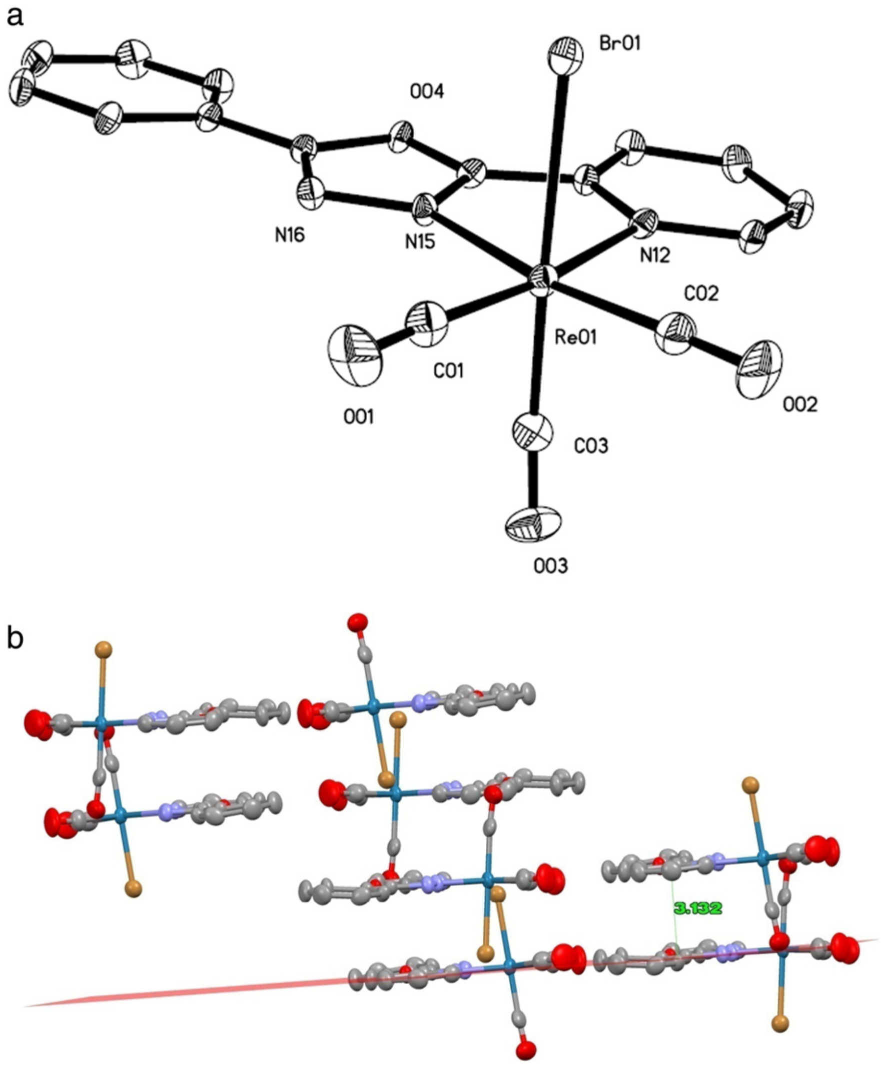

Fig. 1. A. Single crystal structure of Re$(CO)_3$(POP)Br. B. Π-stacking pattern in Re$(CO)_3$(POP)Br crystal.

listed in Table S1 (Supporting Information). Re(I) center is localized at the center of a distorted octahedral coordination field with key structural parameters comparable to literature values [14–16]. Owing to the electronic difference between two coordination N atoms, the two Re–N bond length values are not exactly the same. It seems that the coordination attraction between Re(I) center and N(15) is stronger than that between Re(I) center and N(12). This can be explained by the short conjugation chain and the electron-donating atoms in oxadiazole ring. The three Re–C bonds are slightly different from each other, suggesting that they are adjusting themselves to meet an optimal coordination with Re(I) center. Most bite angles in Table S1 are close to 90°, except for N(12)–Re(01)–N(15). This bite angle is smaller than those in tetrahedral field [14–16]. It is thus concluded that there is roomy space around Re(I) center in Re$(CO)_3$(POP)Br, owing to the small steric hindrance of ligands CO and Br. This decreased steric hindrance may favor sensing procedure as abovementioned.

Our desired large conjugation plane in POP ligand is confirmed by π-stacking pattern in Re$(CO)_3$(POP)Br crystal. As shown in Fig. 1B, free rotation of σ bonds in POP ligand makes its three rings coplanar, showing a large conjugation plane. Π-π attraction between these conjugation planes makes Re$(CO)_3$(POP)Br molecules take a highly ordered array. In this case, POP planes of Re$(CO)_3$(POP)Br molecules align nearly parallel to each other with minimal distance of 3.132 Å, confirming the π–π attraction between them. Such π-stacking in solid state has been proved positive to improve emissive performance by suppressing structural relaxation that happens in excited state, resulting in long emission lifetime, high emission yield and emission blue shift [16,19]. Such π-stacking, however, should be eliminated in sensing application since it blocks analyte attack.

3.2. Electronic structure of probe Re$(CO)_3$(POP)Br

Considering that oxygen sensing procedure is accomplished through a dynamic collision between O_2 molecules and probe excited state, electronic nature of Re$(CO)_3$(POP)Br should be cleared [11,12]. Density functional theory calculation has been proved talented on exploring electronic structure of transition metal complexes and thus used here to understand Re$(CO)_3$(POP)Br electronic nature [13–16]. Percentage composition of its first ten singlet excitations and corresponding frontier molecular orbitals (MOs) is listed in Tables S2 and S3 (Supporting Information). It is observed that the onset electronic transitions are those from occupied frontier MOs to unoccupied ones. Occupied frontier MOs have obvious metal character, admixed with contributions from Br and other ligands. While unoccupied frontier MOs are essentially π* of POP ligand. Electronic transitions between occupied and unoccupied frontier MOs are thus assigned as a mixed character of metal-to-ligand-charge-transfer (MLCT) and ligand-to-ligand-charge-transfer (LLCT) [16]. Upon excitation, ground state electrons of Re(I) center is

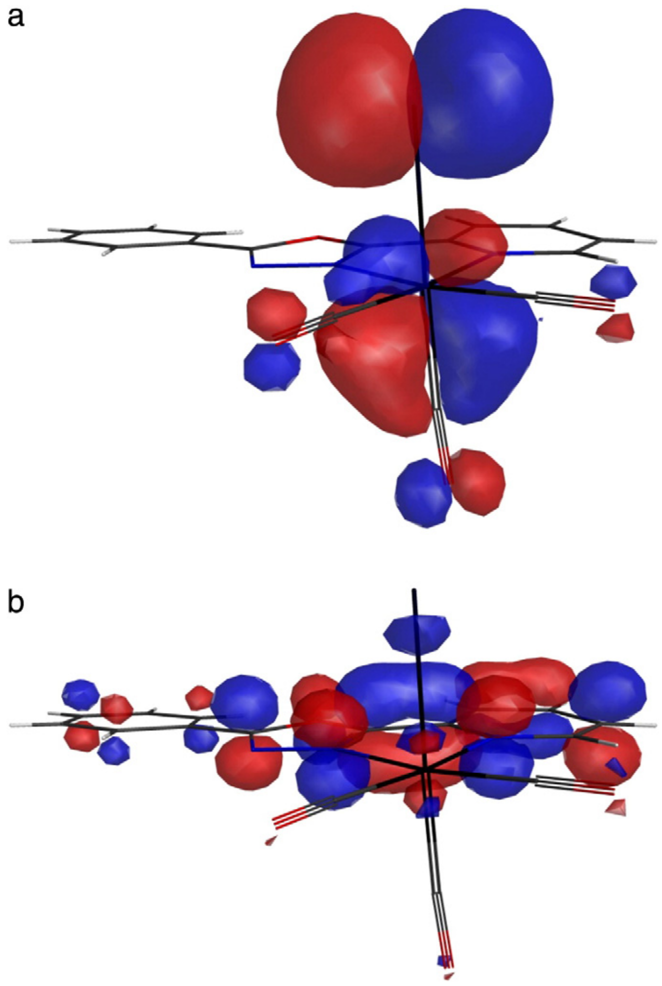

Fig. 2. Frontier molecular orbitals of $Re(CO)_3(POP)Br$ (a, HOMO; b, LUMO).

migrated to π* of POP ligand, as shown in Fig. 2. Owing to heavy metal turbulence effect, such MLCT/LLCT excited sate is anticipated to have a triplet nature with lifetime as long as a few microseconds, offering enough collision chances for O_2 attack.

3.3. Photophysical feature of probe $Re(CO)_3(POP)Br$

3.3.1. Absorption and excitation

UV–vis absorption and excitation spectra of $Re(CO)_3(POP)Br$ in CH_2Cl_2 (10 μM) are shown in Fig. 3. There are three major bands in its absorption spectrum: two strong ones peaking at 232 nm and 288 nm and a broad weak one ranging from 360 nm to 500 nm, respectively. The former two bands are similar to those of free POP ligand shown in Fig. 3 and thus are attributed to ligand π → π* (ILCT) transition. The weak broad absorption band is a new one compared to the absorption spectrum of free POP ligand. Taking above theoretical calculation result into account, this weak band is attributed to MLCT/LLCT absorption [15]. This low energy band is quite similar to that of Re(I) complex $Re(CO)_3(Phen)Br$, where Phen = 1,10-phenanthroline [15,16]. Above analysis has confirmed that there is a large coplanar conjugation plane in POP ligand. But the absorption edge of $Re(CO)_3(POP)Br$ has been well preserved even though its conjugation plane is larger than that in $Re(CO)_3(Phen)Br$. We attribute its causation to the confinement effect from oxadiazole ring [16].

The excitation spectrum of $Re(CO)_3(POP)Br$ shown in Fig. 3 suggests, however, that the two high energy bands don't excite emissive center effectively, while the weak absorption band does. This fact becomes rational considering the following factors. Molar distinction coefficient of charge transfer transitions is much lower than that of π → π* transition. But charge transfer transitions are efficient in exciting emissive center since emissive center of $Re(CO)_3(POP)Br$ is derived from its first onset electronic transition. Π → π* excited state has to experience a series of energy-wasting procedures before transferring its energy to emissive center, leading to its low excitation efficiency [16].

3.3.2. PL emission and decay lifetime

Emission spectrum of $Re(CO)_3(POP)Br$ in CH_2Cl_2 (10 μM) is shown in Fig. 4. This emission band peaks at 545 nm with FWHM of 74 nm, showing no vibronic progressions. Here FWHM means full width at half maximum. The Stokes shift between absorption edge (500 nm) and emission peak (545 nm) is as large as 45 nm. These characters suggest that the emissive center indeed has a charge transfer character, which is consistent with above theoretical analysis [15,16]. For comparison, $Re(CO)_3(Phen)Br$ emission peaks at 554 nm with FWHM of 90 nm [15]. Stokes shift value of $Re(CO)_3(POP)Br$ is found smaller than literature values of Re(I) and Cu(II) complexes [14–16]. It is thus concluded that the structural relaxation of $Re(CO)_3(POP)Br$ excited state is limited owing to the small ligand steric hindrance in $Re(CO)_3(POP)Br$. In addition, the confinement effect from oxadiazole ring might contribute to this limited structural relaxation in $Re(CO)_3(POP)Br$ excited state.

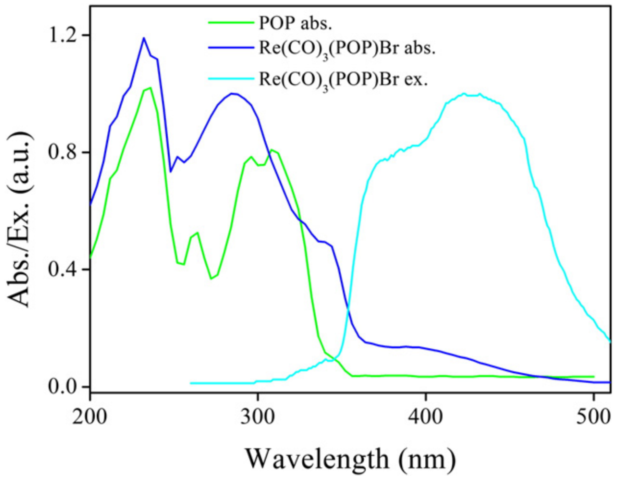

Fig. 3. UV–vis absorption (abs.) and excitation (ex.) spectra of $Re(CO)_3(POP)Br$ and POP in CH_2Cl_2 (10 μM).

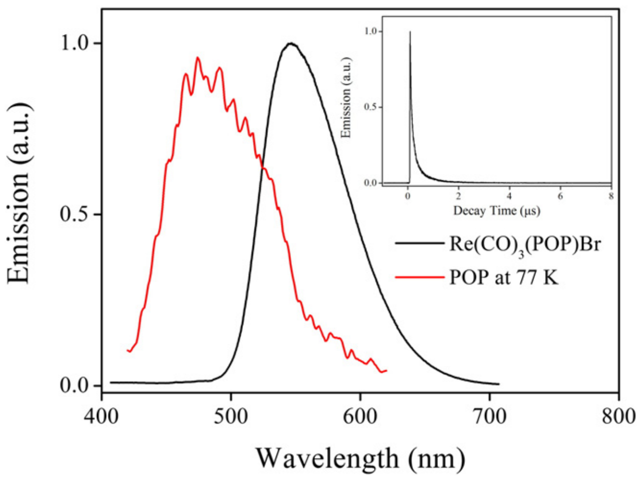

Fig. 4. Emission spectrum of $Re(CO)_3(POP)Br$ in CH_2Cl_2 (10 μM) and POP under 77 K (λ_{ex} = 355 nm). Inset: emission decay dynamics of emission decay dynamics.

For a better understanding on $Re(CO)_3(POP)Br$ emissive center, its emission decay dynamics are recorded and shown as the inset of Fig. 4. Biexponential decay pattern is observed with $\tau_1 = 0.369$ μs ($A_1 = 0.355$) and $\tau_2 = 0.0668$ μs ($A_2 = 2.420$), respectively. These two long-lived emissive components suggest their phosphorescent nature. They are thus attributed to triplet states of MLCT and LLCT. According to a literature report, the observation of strong absorption in $\pi \rightarrow \pi^*$ region and a short-lived decay component suggests an efficient potential surface crossing from $\pi \rightarrow \pi^*$ state to MLCT state [15]. We thus attribute the short-lived component τ_2 to the radiative decay of $\pi \rightarrow \pi^*$ state, while the long-lived component τ_1 to the radiative decay of MLCT state. This assignment is consistent with their electronic nature.

Emission yield of $Re(CO)_3(POP)Br$ in CH_2Cl_2 (10 μM) is determined as 0.033 following a literature method [19]. This value seems unsatisfactory compared to those of superior emitters [13–16]. Corresponding radiative (K_r) and non-radiative (K_{nr}) constants are calculated as $0.1633 \times 10^6\ s^{-1}$ and $4.785 \times 10^6\ s^{-1}$, respectively, with Eqs. (1)–(3). It is clear that the emissive center is dominated by non-radiative decay, resulting in its unsatisfactory emission yield. Generally, there are two possible non-radiative decay paths for a MLCT excited state: one is structural relaxation, the other is electronic configuration from ^{3}MLCT state to ^{3}LC (ligand centered) state, as suggested by Zhang and coworkers [16]. ^{3}LC level of POP ligand is determined as 476 nm which is much higher than ^{3}MLCT energy (545 nm) by its low temperature phosphorescence spectrum shown in Fig. 4. This fact denies the possibility of electronic configuration from ^{3}MLCT state to ^{3}LC state. It is hereby confirmed that $Re(CO)_3(POP)Br$ emission is originated from ^{3}MLCT state, with no ligand ^{3}LC emission. Thus, structural relaxation that happens in $Re(CO)_3(POP)Br$ is the dominant non-radiative decay path. This fact is consistent with the small ligand steric hindrance in $Re(CO)_3(POP)Br$.

$$\Phi = \frac{K_r}{K_r + K_{nr}} \tag{1}$$

$$\frac{1}{\tau} = K_r + K_{nr} \tag{2}$$

$$\tau = \frac{A_1 {\tau_1}^2 + A_2 {\tau_2}^2}{A_1 \tau_1 + A_2 \tau_2}. \tag{3}$$

3.4. Morphology and characterization of $Re(CO)_3(POP)Br$ doped MCM-41

For a typical sensing system, probe molecules are usually dispersed in supporting matrix to allow smooth and fluent diffusion [1,2,11,12]. Here MCM-41 is chosen as supporting matrix owing to its highly ordered hexagonal tunnels which favor both high diffusion coefficient of analyte and uniform distribution of probe [11,12]. As a start, three doping concentrations of 40 mg/g, 45 mg/g, and 50 mg/g are tried for performance optimization. Small angle X-ray diffraction (SAXRD) patterns of the three composite samples and blank MCM-41 are shown in Fig. 5. Three well-resolved Bragg reflection peaks indexed as d_{100}, d_{110}, and d_{200} are observed for blank MCM-41, which is consistent with those of standard MCM-41 sample [11,12]. After loading $Re(CO)_3(POP)Br$, these Bragg reflection peaks are well preserved with no spectral shift or widening, despite of their various intensity values. It is thus confirmed that these hexagonal tunnels have been well preserved after probe loading procedure.

Absorption and solid state diffuse reflection spectra of a representative sample (45 mg/g) are recorded and shown as Fig. 6, along with those of blank MCM-41 for comparison. Blank MCM-41 shows slim absorption all over the whole UV–vis region. Its diffuse reflection is strong with no obvious variation, which is consistent with its absorption spectrum. As for the representative sample (45 mg/g), its absorption is quite similar to that of $Re(CO)_3(POP)Br$ in CH_2Cl_2, with absorption peaks of 244 nm, 284 nm and 369 nm, respectively. Correspondingly, there are two low reflection regions peaking at 261 nm and 364 nm, respectively, as shown by the solid state diffuse reflection spectrum. It is thus confirmed that $Re(CO)_3(POP)Br$ has been attached to MCM-41 matrix.

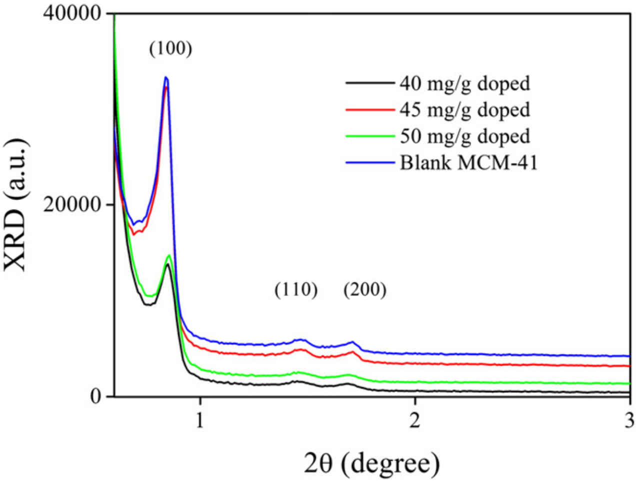

Fig. 5. SAXRD patterns of $Re(CO)_3(POP)Br$ doped MCM-41 (40 mg/g, 45 mg/g and 50 mg/g) and blank MCM-41.

N_2 adsorption and desorption measurement is performed on a representative sample (45 mg/g) and pure MCM-41. Surface area, pore volume and pore size of pure MCM-41 are determined as 738.22 m^2/g, 0.579 cm^3/g, and 2.51 nm, respectively (Figure S1, Supporting Information). While, those for the representative sample (45 mg/g) are decreased to 405.36 m^2/g, 0.2511 cm^3/g, and 2.22 nm, respectively (Figure S1, Supporting Information). It is thus confirmed that our dopant molecules have been doped into MCM 41 tunnels, not attached onto their surface.

3.5. Sensing performance of $Re(CO)_3(POP)Br$ doped MCM-41

3.5.1. Sensitivity

Oxygen sensing performance of $Re(CO)_3(POP)Br$ doped MCM-41 is evaluated by their emission response to various O_2 concentrations as follows. Pure MCM-1 is non-emissive, which means that composite emission in Fig. 7 comes from dopant $Re(CO)_3(POP)Br$. Emission shape of these composite samples is slightly different from that of

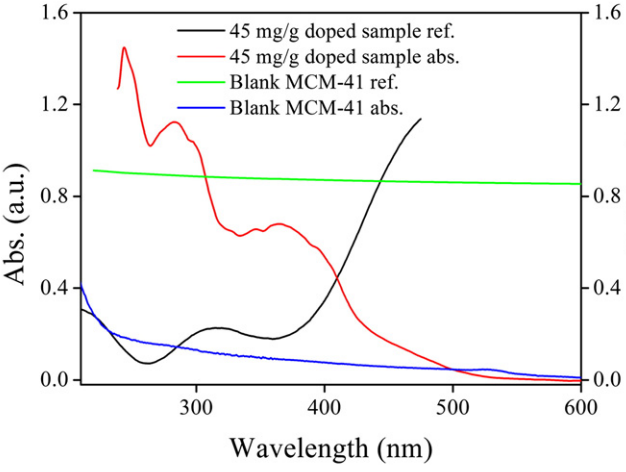

Fig. 6. Absorption (abs.) and solid state diffuse reflection (ref.) spectra of a representative sample (45 mg/g) and a blank MCM-41.

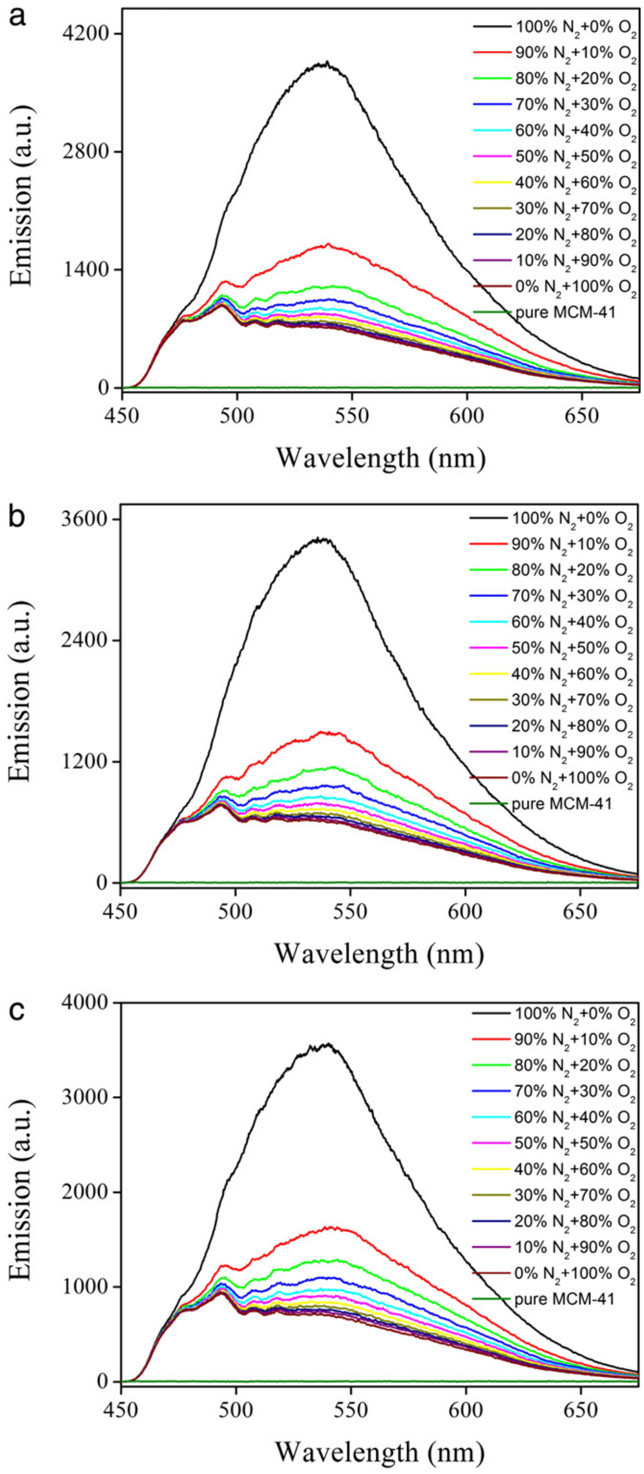

Fig. 7. Emission spectra of the 40 mg/g doped sample upon oxygen concentration varying from 0% to 100% (interval = 10%). B. Emission spectra of the 45 mg/g doped sample upon oxygen concentration varying from 0% to 100% (interval = 10%). C. Emission spectra of the 50 mg/g doped sample upon oxygen concentration varying from 0% to 100% (interval = 10%).

pure $Re(CO)_3(POP)Br$, which may be explained by matrix local confinement effect known as rigidochromism [11,12]. Emission intensity of the three composites decreases obviously with increasing O_2 concentrations, indicating that their emission is quenchable by O_2 molecules. For discussion convenience, maximum sensitivity is defined as the ratio of I_0/I_{100}, where I_0 and I_{100} are emission intensity values in pure N_2 atmosphere and pure O_2 atmosphere, respectively. Sensitivity values, along with other key sensing parameters, are summarized in Table 1. These values are found comparable to or even slightly higher than literature values of similar sensing composites, which can be explained by below factors [11,12,14–17]. First, there is a large coplanar conjugation plane in our probe which may increase electronic distribution and lifetime of excited electrons, increasing collision probability between excited probe and analyte. Second, the ligand steric hindrance in $Re(CO)_3(POP)Br$ is slim, favoring O_2 attack. Third, the highly ordered tunnels of matrix guarantee efficient analyte transportation and diffusion, facilitating O_2 sensing.

In MCM-41 matrix, probe emission blue shifts to 536 nm, compared to that in CH_2Cl_2 (545 nm), which can be explained by rigidochromism [11,12]. FWHM value is slightly increased to ~93 nm, compared to that in CH_2Cl_2 (74 nm). It seems that $Re(CO)_3(POP)Br$ excited state has been restricted in MCM-41 matrix, leading to decreased structural relaxation and widened emission band. Another phenomenon worthy of more explanation words is the fact that there is an optimal doping concentration in these composites. The 45 mg/g doped sample shows the highest sensitivity. Either a higher or a lower doping concentration decreases sensitivity. It is thus assumed that there are two or more factors controlling sensitivity: one is the amount of probe molecules, the other is their self-absorption/self-quenching. By increasing probe amount, emission intensity is certainly increased, leading to high sensitivity. On the other hand, self-absorption/self-quenching becomes serious upon high probe concentration, compromising emission intensity as well as sensitivity [14,17]. These two factors may get a balance in the 45 mg/g doped sample, resulting in its highest sensitivity.

3.5.2. Stern–Volmer curves

Aiming at a better understanding on this sensing procedure, emission decay dynamics of a representative sample (45 mg/g doped) under pure N_2, pure O_2 and air conditions are recorded and shown as the inset of Fig. 8. Similar to the case of $Re(CO)_3(POP)Br$ in CH_2Cl_2, emission of the 45 mg/g doped sample follows biexponential decay pattern with mean lifetimes of 5.26 μs in air ($A_1 = 0.07623$, $\tau_1 = 7.37$ μs, $A_2 = 0.17302$, $\tau_2 = 2.40$ μs, $R^2 = 0.995$), 11.33 μs in pure N_2 ($A_1 = 0.33934$, $\tau_1 = 2.00$ μs, $A_2 = 0.37347$, $\tau_2 = 12.6723$ μs, $R^2 = 0.996$) and 4.5 μs in pure O_2 ($A_1 = 0.16655$, $\tau_1 = 2.05$ μs, $A_2 = 0.06070$, $\tau_2 = 6.60$ μs, $R^2 = 0.996$), respectively, as calculated by Formula 3. These long-lived lifetimes suggest their triplet nature, which further confirms the successful probe loading. It seems that being immobilized in matrix increases emission lifetime, as explained by rigidochromism. This observation is consistent with abovementioned emission blue shift. It is clear that the presence of O_2 decreases composite lifetime obviously, which is consistent with literature reports [11,12]. We thus come to a conclusion that probe emission is quenched by O_2 molecules through a dynamic collision mechanism, as described by Eq. (4), where "*" means an excited state.

$$\text{Re(I)-probe}*+{}^{3}O_2\rightarrow\text{Re(I)-probe}+{}^{1}O_2*. \tag{4}$$

Table 1
Oxygen sensing parameters of the three composite samples.

Sample	λ (nm)	I_0/I_{100}	K_{SV1} ($O_2\%^{-1}$)	K_{SV2} ($O_2\%^{-1}$)	f_{01}	f_{02}	R^2	T_{res} (s)	T_{rec} (s)
40 mg/g	536	5.33	0.2204	0.0009	0.8351	0.1649	0.9987	7	54
45 mg/g	537	5.54	0.2093	0.0023	0.8267	0.1733	0.9995	6	56
50 mg/g	539	5.02	0.1993	0.0030	0.7945	0.2055	0.9987	7	57

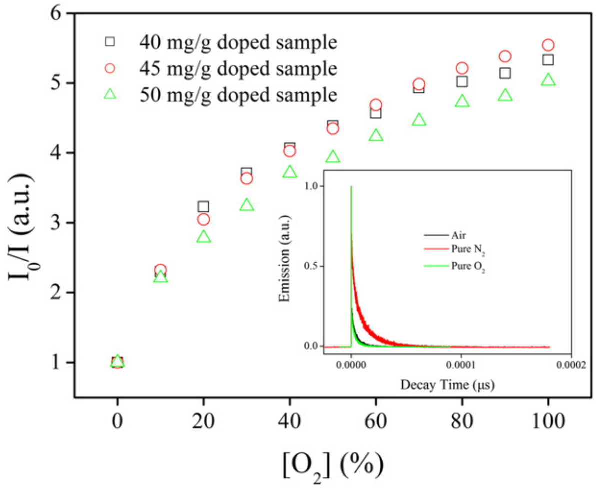

Fig. 8. Stern–Volmer curves of $Re(CO)_3(POP)Br$ doped MCM-41 (40 mg/g, 45 mg/g and 50 mg/g). Inset: emission decay dynamics of a representative sample (45 mg/g) under pure N_2, pure O_2 and air conditions.

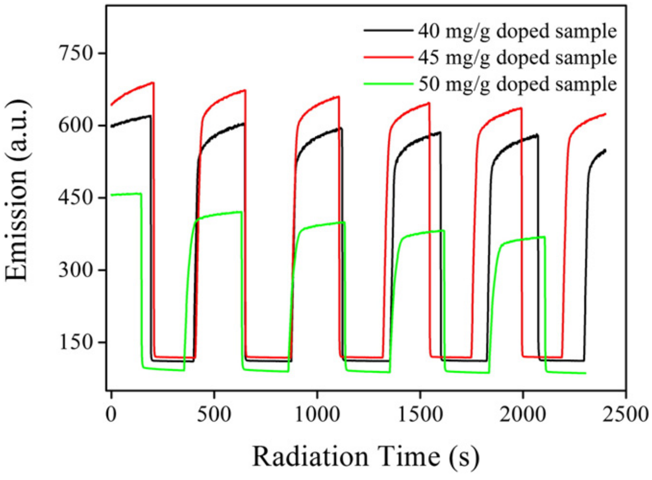

Fig. 9. Emission monitoring of $Re(CO)_3(POP)Br$ doped MCM-41 (40 mg/g, 45 mg/g and 50 mg/g) when atmosphere is periodically changed between 100% N_2 and 100% O_2.

With this dynamic sensing mechanism confirmed, emission response of these composite samples to various O_2 concentrations is further analyzed. If probe molecules are uniformly distributed in matrix and their emission follows a dynamic quenching mechanism, intensity form of Stern–Volmer equation can be described as Eq. (5). Here I and I_0 are emission intensity value and that in pure N_2 atmosphere, respectively. K_{SV} and $[O_2]$ are Stern–Volmer constant and O_2 concentration, respectively [11,12]. An ideal Stern–Volmer curve is supposed to be a linear one with slope of K_{SV}, which, however, is not the case for our Stern–Volmer curves shown in Fig. 8. A more complicated mode should be proposed.

$$I_0/I = 1 + K_{SV}[O_2]. \tag{5}$$

Assuming that there are two or more species of sites in our composites, only one of them is sensitive to O_2, the others are not. In this case, Stern–Volmer equation should be modified by taking contribution of each site into account, as shown by Eq. (6). Here $f_{1,}$ f_2, K_{SV1} and K_{SV2} are fractional contributions and corresponding Stern–Volmer constants of sensing sites, respectively [11,12]. This two-site model can well fit our working curves, as shown by Fig. 8. Sensing parameters listed in Table 1 suggest that K_{SV2} is smaller than K_{SV1} by two orders of magnitude, indicating that site-2 is nearly immune to O_2 molecules, leading to non-linearity and compromised sensitivity of Stern–Volmer curves. We attribute site-2 to the “deep-corner” in composites which are impenetrable by O_2 diffusion. For further improvement, such “deep-corner” should be eliminated or minimized.

Considering that all K_{SV2} values are smaller than K_{SV1} values by two orders of magnitude, Formula 6 can be simplified with K_{SV2} set as “0”. Corresponding fitting parameters are listed in Table S4 (Supporting Information). It is observed that this simplified model can well describe Stern–Volmer curves.

$$\frac{I_0}{I} = \frac{1}{\dfrac{f_1}{1 + K_{SV1}pO_2} + \dfrac{f_2}{1 + K_{SV2}pO_2}}. \tag{6}$$

3.5.3. Response/recovery time and photostability

Response and recovery character of our composites is evaluated by monitoring their emission when atmosphere is periodically switched between 100% N_2 and 100% O_2, as shown in Fig. 9. It is clear that emission intensity is dependent on O_2 presence. In pure N_2 atmosphere, emission maximum is well preserved, showing no obvious photobleaching. Upon pure O_2 atmosphere, emission is greatly quenched. Response and recovery cycle can be quickly finished with no hysteresis. For discussion convenience, response time is defined as the time taken by a sample to decrease to 5% of its emission maximum when atmosphere is switched from pure N_2 to pure O_2 [11,12]. Similarly, recovery time is defined as the time taken by a sample to increase to 95% of its emission maximum when atmosphere is switched from pure O_2 to pure N_2. These values are summarized in Table 1, which are found comparable to or even shorter than literature values [11,12]. The following reasons should be claimed responsible for these fast response and recovery times. First, the large coplanar conjugation plane in our probe increases electron distribution and emission lifetime, favoring sensing collision between probe and analyte. Second, there is small steric hindrance for O_2 attack owing to the small ligands in probe. Third, the highly ordered tunnels of MCM-41 guarantees efficient analyte transportation. In addition, it is found that recovery time is obviously longer than response time. This phenomenon is consistent with literature reports, which has been explained by diffusion-controlled dynamic response and recovery behavior [11,12,14,17,20].

Conclusion

In conclusion, we demonstrated a Re(I) complex for oxygen sensing application. A typical electron-withdrawing group of 1,3,4-oxadiazole was incorporated into POP ligand so that electronic distribution of excited electrons and lifetime of $Re(CO)_3(POP)Br$ could be increased, resulting in more sensing collision chances with O_2 molecules. $Re(CO)_3(POP)Br$ was firstly characterized in detail, including its single crystal structure, electronic nature and photophysical parameters. Its was found that its emission showed a long lifetime for O_2 sensing. By doping $Re(CO)_3(POP)Br$ into MCM-41, oxygen sensing performance of the resulting composites was analyzed and discussed in detail. Dynamic sensing in these composites gave the highest sensitivity of 5.54 and a short response time of ~6 s. We attributed these good parameters to the following factors. First, the large coplanar conjugation plane in our probe increased electron distribution and emission lifetime, favoring sensing collision between probe and analyte. Second, there was small steric hindrance for O_2 attack owing to the small ligands in probe. Third, the highly ordered tunnels of matrix guaranteed efficient analyte transportation. There were drawbacks to solve though. The “deep-corner” in composites should be minimized or eliminated so that sensitivity could be further improved with a linear Stern–Volmer working curve.

Acknowledgment

The authors gratefully thank our universities for their equipments and financial support.

Appendix A. Supplementary data

Supplementary data to this article can be found online at http://dx.doi.org/10.1016/j.saa.2015.09.034.

References

[1] Y. Guo, L. Zhang, S. Zhang, Y. Yang, X. Chen, M. Zhang, Biosens. Bioelectron. 63 (2015) 61–71.

[2] D. Sarkar, A. Pramanik, S. Jana, P. Karmakar, T.K. Mondal, Sensors actuators B 209 (2015) 138–146.

[3] M.R. Awual, M.M. Hasan, M.A. Khaleque, Sensors actuators B 209 (2015) 194–202.

[5] O.S. Wolfbeis, Anal. Chem. 80 (2008) 4269–4283.

[6] C. Baleizao, S. Nagl, M. Schaferling, M.N. Berberan-Santos, O.S. Wolfbeis, Anal. Chem. 80 (2008) 6449–6457.

[7] L.C. Clark Jr., Trans. Am. Soc. Artif. Intern. Organs. 2 (1956) 41–48.

[8] L.W. Winkler, Ber. Dtsch. Chem. Ges. 21 (1888) 2843–2855.

[9] G. Zhang, J. Chen, S.J. Payne, S.E. Kooi, J.N. Demas, C.L. Fraser, J. Am. Chem. Soc. 129 (2007) (15728-15728).

[10] A. Gulino, S. Giuffrida, P. Mineo, M. Purrazzo, E. Scamporrino, G. Ventimiglia, M.E. Van der Boom, I. Fragala, J. Phys. Chem. B 110 (2006) 16781–16786.

[11] B. Lei, B. Li, H. Zhang, L. Zhang, W. Li, J. Phys. Chem. C 111 (2007) 11291–11301.

[12] B. Lei, B. Li, H. Zhang, S. Lu, Z. Zheng, W. Li, Y. Wang, Adv. Funct. Mater. 16 (2006) 1883–1891.

[13] L. Yang, J.K. Feng, A.M. Ren, M. Zhang, Y.G. Ma, X.D. Liu, Eur. J. Inorg. Chem. 10 (2005) 1867–1879.

[14] J. Jia, Y. Tian, Z. Li, Synth. Met. 161 (2011) 1377–1382.

[15] Z. Si, X. Li, X. Li, H. Zhang, J. Organomet. Chem. 694 (2009) 3742–3748.

[16] L. Zhang, S. Yue, B. Li, D. Fan, Inorg. Chim. Acta 384 (2012) 225–232.

[17] L. Shi, B. Li, S. Yue, D. Fan, Sensors actuators B Chem. 137 (2009) 386–392.

[18] M. Kranenburg, Y.E.M. van der Brugt, P.C.J. Kamer, P.W.N.M. van Leeuwen, Organometallics 14 (1995) 3081–3089.

[19] L. Zhang, B. Li, Z. Su, Langmuir 25 (2009) 2068–2074.

[20] S.M. Kuang, D.G. Cuttell, D.R. McMillin, P.E. Fanwick, R.A. Walton, Inorg. Chem. 41 (2002) 3313–3322.